Real-Time Holographic Tracking and Control of Microrobots

Ayoung Hong, Burak Zeydan, Samuel Charreyron, Olgaç Ergeneman, Salvador Pané, M. Fatih Toy,
Andrew J. Petruska, and Bradley J. Nelson

Abstract—Digital holography is used to track the three-dimensional position of a magnetic microrobot maneuvered in real time by means of an electromagnetic manipulation system. The method presented is able to process holograms at 40 Hz with a position accuracy in the imaging plane and in depth of ± 23 and ± 180 μm, respectively. As this method does not require magnification, microrobots can be tracked in significantly larger working volumes than conventional optical methods. The performance of this tracking method is demonstrated by visually servoing a magnetic bead around a cubic trajectory.

Index Terms—Micro/Nano robots, visual servoing, localization, automation at micro-nano scales.

I. INTRODUCTION

MICROROBOTS have been proposed as dexterous machinery for lab-on-a-chip devices in applications ranging from single cell mechanical characterization, to mobile localized mixing and assembly, targeted drug delivery, and microassembly [1]–[4]. While many aspects of microrobotics, such as locomotion, fabrication, and functionalization, have been thoroughly addressed, visual servoing of mobile microrobots has primarily been restricted to two-dimensions (2D). Some notable exceptions exist. For example, 2D heading and 3D position control of untethered magnetic microrobots for ophthalmic applications has been demonstrated [5], [6], 3D control of multiple magnetic microscale structures has been demonstrated [7], the self-propelled catalytic microjets have been steered in 3D using magnetic guidance [8], and three-dimensional simultaneous manipulations of multiple microscale particles have been achieved with optical traps [9]. Still, these examples are significantly outnumbered by their 2D counterparts, primarily because of technical difficulties in tracking microrobots in 3D.

Currently, there are two methods for extracting the 3D position of a microrobot during manipulation: stereo vision and depth-from-focus. As in larger systems, stereo vision provides
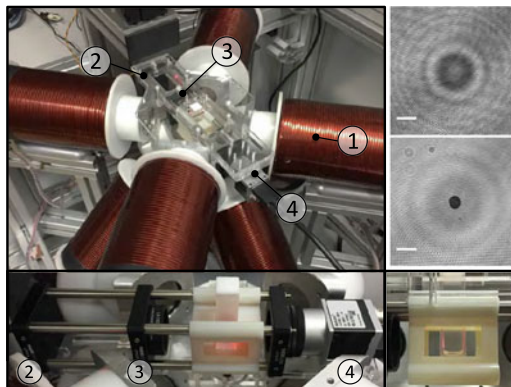
Fig. 1. Digital in-line holography integrated with an electromagnetic manipulation system ① [5]. The in-line holographic setup consists of a monochromatic laser source ②, a collimating lens ③, and a digital camera ④ without microscopic objectives. The hologram of a 100 μm size bead in the deionized water is captured and its in-focus image is numerically reconstructed with a depth, $d = 68.2$ mm. Scalebars: 200 μm.

an intuitive method to reconstruct the 3D position of an object. For example, the 3D closed-loop control of microobjects has been accomplished using two optical microscopes from the top and the side [8], [10]. Unfortunately, the high magnification systems required to image microrobots suffer from a reduced depth-of-field [11]. When applied to stereo vision, this results in a very limited observable volume. To avoid this problem or to implement tracking when only one viewing angle is available, depth-from-focus can be used [12], [13]. This method estimates the depth of the object based on the extent that it is out of focus and can adjust the focusing depth to move with the microrobot as it moves in 3D space. Unfortunately, it is only able to simultaneously track objects at a single depth.

The physical and life sciences have overcome these limitations by using digital holography. Digital in-line holography reconstructs a 3D volume based on the diffraction pattern created when an electromagnetic wave interacts with an object [14], [15]. This diffraction pattern can be numerically analyzed to yield image slices at any desired imaging depth, which enables volumetric image reconstruction similar to magnetic resonance imaging. Holographic imaging was first proposed in 1948 to eliminate the lenses and the aberration introduced by them in electron beam imaging systems [16]. It was then adapted for optical microscopy in 1992 [17] and has found many applications ranging from high-resolution imaging and volume estimation of living cells [18], [19], to 3D tracking of motile biological cells [20]–[22], bubbles in air-water mixtures [23], and particles in colloids [24]. However, due to the expensive computational cost of the approach, additional efforts have been made to
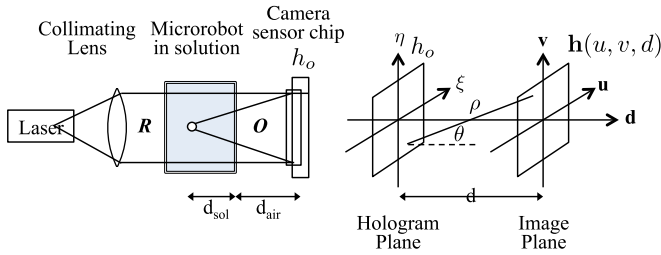
Fig. 2. Schematic of a digital in-line holography setup. R, reference wave; O, object wave; d, propagation distance; d_{sol} and d_{air}, geometric distance of wave travelling through solution and air, respectively. h_0 is a recorded hologram function in a hologram plane with a camera sensor chip and $\mathbf{h}(u, v, d)$ is a complex amplitude field in the image plane, which is the reconstructed image of the recorded hologram at a desired propagation distance d. ξ, η, u, and v are the spatial coordinates in the hologram plane and the image plane.

achieve real-time holographic imaging and reconstruction. Accelerated autofocusing has been proposed by using resampling of the complex wave field [25] or scaled holograms [26], and fast reconstruction by using a graphics processing unit (GPU) [27], [28]. Nevertheless, real-time particle extraction or 3D object localization based on holography has yet to be reported.

In this paper, we have integrated a digital holographic microscope with a 5-DOF electromagnetic manipulation system to track a microrobot in real-time (>20 Hz) for closed-loop position control (see Fig. 1). The remainder of the paper will be structured as follows. First, the mathematical background for holographic reconstruction is presented and the techniques required to achieve holographic tracking in real-time for micromanipulation will be discussed. Then, the calibration and use of a holographic system to track magnetic microrobots in a magnetic manipulation system will be presented. Finally, we will conclude with a discussion of the utility of digital-in-line-holography for general microrobotic applications and a summary of our findings.

II. DIGITAL IN-LINE HOLOGRAPHY BACKGROUND

A holographic imaging setup consists of a coherent collimated reference source R and a camera sensor chip (Fig. 2). When the reference wave R interacts with an object in the workspace, a diffraction wave O is generated. The interference pattern recorded by the camera sensor chip h_0, encodes all of the spatial information of the object in the 3D workspace. Holographic reconstruction is performed by backpropagating the hologram h_0 with the Fresnel diffraction pattern. The resulting object wave provides a reconstruction of the object's diffraction pattern at any depth.

The numerical hologram reconstruction is based on the Fresnel–Kirchhoff integral [29], which describes the complex amplitude image $\mathbf{h}(u, v, d)$ as

$$\mathbf{h}(u, v, d) = \frac{i}{\lambda} \iint h_0 R \frac{\exp(-i\frac{2\pi}{\lambda}\rho)}{\rho} \times (\frac{1}{2} + \frac{1}{2}\cos\theta)\mathrm{d}\xi\mathrm{d}\eta \tag{1}$$

with

$$\rho = \sqrt{d^2 + (\xi - u)^2 + (\eta - v)^2} \tag{2}$$

where λ is the laser wavelength, ρ is the distance between a point in the hologram plane and a point in the reconstructing image plane [29], and θ is the angle between two points. For large values of d the small angle approximation ($\cos\theta \approx 1$) can be applied and the reference wave R can be modelled as constant and real valued[30]. The convolution described by (1) is more efficiently implemented in the Fourier domain. Thus, the reconstruction process is given by a Fourier transform, an element-wise multiplication, and an inverse Fourier transform:

$$\mathbf{h}(u, v, d) = \mathcal{F}^{-1}\{\mathcal{F}\{h_0\} \times G_d\}, \tag{3}$$

where $\mathcal{F}$ is the Fourier transform operator and G_d is the distance dependent kernel that selects the reconstruction depth

$$G_d = \exp(i\frac{2\pi}{\lambda}) \exp(-i\pi\lambda d(u_s^2 + v_s^2)). \tag{4}$$

In (4), u_s and v_s represent the Fourier spectral coordinates. The numerical aperture (N.A.) of the system is

$$N.A. = n(1 + 4(d/w)^2)^{-1/2} \tag{5}$$

where w is the sensor size and n is the refractive index of the medium. The axial resolution of the reconstruction is

$$\sigma_{\text{axial}} = \frac{\lambda}{(N.A)^2} = \frac{\lambda}{n^2}(1 + 4(d/w)^2), \tag{6}$$

which describes the ability to resolve two different objects at different depths [15].

The complex amplitude image $\mathbf{h}$ can be reconstructed at any distance d. However, this distance is the effective displacement in vacuum. Since the wave propagates in optically dense mediums, i.e., when the refractive index of medium is not unity, the propagation distance, d, is given by

$$d = \Sigma \frac{d_i}{n_i}, \tag{7}$$

where d_i and n_i are the geometric distances and the refractive indexes of the ith medium, respectively.

III. TRACKING ALGORITHM

The numerical reconstruction given by (3) defines a set of images that can be searched to determine the 3D position of the microrobot. To accomplish this search, the 3D tracking algorithm is split into three steps, which are presented in Fig. 3. First, the object is located in a raw image and a subimage is generated at the last known depth. Next, a search is conducted to find the current depth of the object. Finally, the object's in-plane position is refined based on the image reconstructed at the current depth.

A. Image Preprocessing

An element-wise multiplication and an inverse Fourier transform in (3) are iteratively performed until the optimum is found. This algorithm has a computational complexity of $O(N^2 \log N)$ where the image is $N \times N$ pixels. Thus, the first step is to crop the image to a smaller region of interest that contains all of the pertinent information. This is performed in two steps: the object
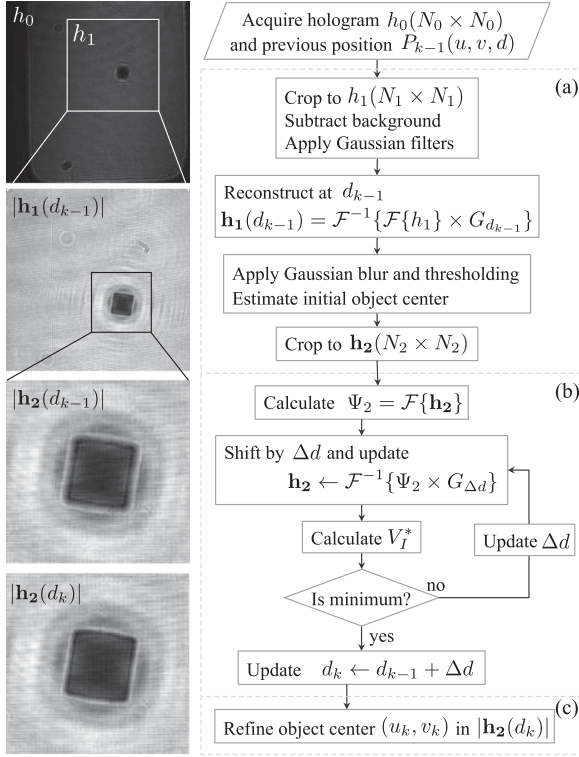
Fig. 3. Flowchart for the holographic tracking algorithm. (a) Preprocessing and initial estimation select a sub-image to use for a numerical reconstruction based on the previous position. (b) Axial position is determined by successively checking the variance of complex image V_I^* using Brent's minimization method. (c) Lateral position is determined by segmenting the object in the final reconstructed image $|\mathbf{h_2}(d_k)|$. $N_0 = 2048$, $N_1 = 1024$, $N_2 = 256$ are used for the experiment.
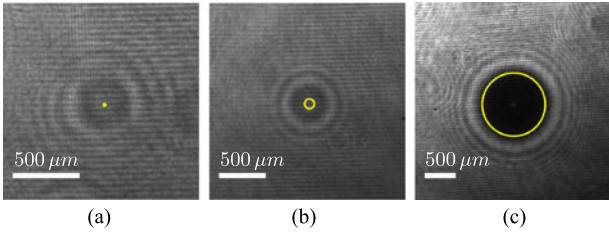

Fig. 4. Holograms of different size of beads in deionized water with diameters of (a) 20 μm, (b) 100 μm and (c) 1000 μm. The actual bead size is marked with circles. These holograms are acquired with a CMOS sensor chip with a pixel size of 5.5 μm $\times$ 5.5 μm without magnification. Scalebars: 500 μm.

Fig. 5. Variance, V_I, and shifted variance, V_I^*, along a depth direction. The container size sets the physical constraints, d_m and d_M on axial position estimation. V_I shows the dipping characteristics near the in-focus plane (case 1) except when the microrobot is near to the wall of container (case 2) (top). To find the knee point in both case 1 and 2, V_I is shifted with base line (bottom). (The graph is normalized to show the two cases at the same scale).

large objects can be difficult to segment in the raw holographic image because the diffraction pattern distorts the object's shape and the ring pattern is less pronounced. In this paper, a relatively large object used in the experiment, and it has been localized in the reconstructed image.

Once the object's approximate in-plane position is known and the image is reconstructed at the last known depth d_{k-1}, the background reference image is subtracted to remove zero-order disturbances [31], and a Gaussian filter is applied to reduce noise. The resulting complex amplitude image $\mathbf{h_1}(d_{k-1})$ is obtained and cropped to $\mathbf{h_2}(N_2 \times N_2)$, which is centered at the initial in-plane position estimate. As $\mathbf{h_2}$ is used for the subsequent search, the size of N_2 needs to be chosen considering computational efficiency and the accuracy of the result. For efficiency, N_2 should be a power of 2 and as small as possible. For accuracy, N_2 should be large enough to capture the diffraction pattern and to preserve the axial resolution of the subimage, i.e.,

$$N_2 > \frac{2\Delta d}{p} \sqrt{\frac{\lambda}{n^2 \sigma_{\text{axial}} - \lambda}}, \tag{8}$$

where p is a camera pixel size and Δd is the maximum depth difference expected between the initial reconstruction plane and the actual depth.

B. Axial Position Estimation

To estimate the axial position of the microrobot, particle extraction using a complex amplitude is used [32]. This method is based on the observation that the variance of the imaginary part of $\mathbf{h}(u, v, d)$ has a minimum near the in-focus plane and is robust to noise in the numerical reconstruction.

The variance of an imaginary part of $\mathbf{h}$ gives a minimum value in the in-focus plane when the microrobot is not in the proximity of the container side walls. However, when the microrobot is

needs to be identified in the image and the image needs to be reconstructed at a depth close to the object's expected depth. The first step determines the center of the subimage to be used in the search. The second step contracts the holographic diffraction pattern so that a smaller image can be used in the search. Localization of the object in the image can be performed either before the reconstruction using the diffraction pattern directly or after by examining the shape of the object's shadow. Small objects are difficult to localize from in-focus images because they are only a few pixels in extent. However, as shown in Fig. 4, they cast a prominent holographic bulls-eye. Thus, these objects can be localized more easily in the raw holographic image. Although the difference is much less significant than for small objects,
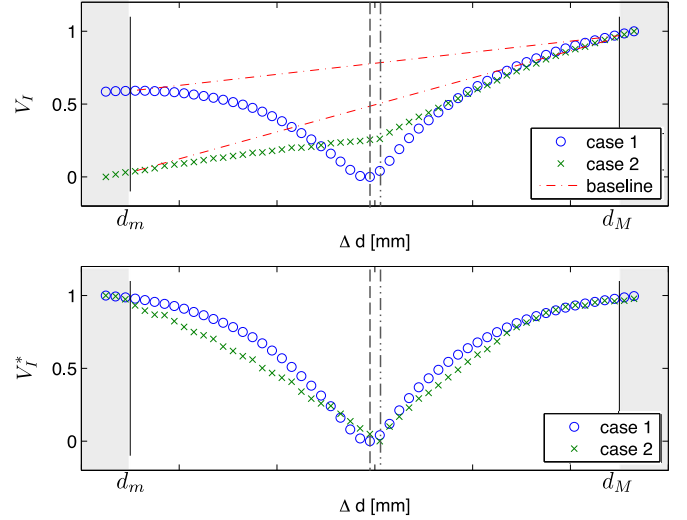
close to the container side walls the hologram is distorted and V_I has a minimum outside of the workspace. In this case, a slope discontinuity is apparent near the in-focus plane (see Fig. 5, case 2). To generalize these two cases, a shifted variance V_I^*, is defined by subtracting the effective variance slope across the container

$$V_I^* = V_I(\Delta d) - \frac{(V_I(d_M) - V_I(d_m))}{(d_M - d_m)}\Delta d \qquad (9)$$

where d_m and d_M are the distance of the front and back of the container. The minimum of the shifted variance V_I^* is slightly different from the minimum of V_I in case 1 or the knee point of V_I in case 2. However, this difference is negligible compared to the size of the microrobot and the uncertainty in the measurement.

Although the minimum can be obtained with an exhaustive search, this is not appropriate for real-time tracking algorithms because of the computational load of calculating V_I^*. Instead, Brent's search method is used to minimize the number of iterations [33]. It combines a bisection method with quadratic interpolation to perform a line search with a minimal number of function evaluations.

The current axial position of the microrobot is updated to $d_k = d_{k-1} + \Delta d$, where Δd is the solution of the minimization problem. The depth d_k is the propagation distance in a vacuum, thus (7) is used to convert it to the geometric axial position of the microrobot as

$$d_k^G = d_k n_{\text{sol}} + \Sigma d_i \left(1 - \frac{n_{\text{sol}}}{n_i}\right) \qquad (10)$$

where n_{sol} is the refractive index of solution, and n_i and d_i are the refractive index and geometrical distance of waves travelling through the ith medium, respectively (see Fig. 2).

C. Lateral Position Estimation

Now that the depth d_k of the microrobot is known, the lateral position estimate (u_k, v_k) can be refined by segmenting the microrobot from the in-focus reconstructed amplitude image $|\mathbf{h}(d_k)|$. This is achieved by applying a Gaussian filter and using adaptive thresholding to segment the object. Among the observed contours in the binary image, the microrobot is segmented by finding the contour that encloses an area that matches the expected object size. The lateral position is then updated with the segmented object's centroid.

IV. EXPERIMENTAL DEMONSTRATION

A. Experimental System

The Octomag electromagnetic manipulation system is used for 3D wireless magnetic control of the microrobot (see Fig. 1) [5]. The system consists of eight electromagnetic coils in a hemispherical arrangement and allows for magnetic fields up to 40 mT and magnetic field gradients up to 1 T/m. The magnetic workspace is a $20 \times 20 \times 20$ mm^3 cube. For holographic imaging, the illumination is produced by a laser diode with a wavelength of 635 nm along with a BP635 red light bandpass filter. A digital camera with 2048×2048 pix-

els, each with an edge length of 5.5 μm, is used to record the holograms. It can generate at 90 fps.

The microrobot is a Neodymium-Iron-Boron (NdFeB) cylindrical magnet with a diameter of 500 μm and a height of 500 μm, which is manipulated in silicone oil. The refractive index of silicone oil (i.e., n_{sol} in (10)), is reported to be 1.502 at 20 °C, taken at the Sodium D Line (589.29 nm wavelength).

The system is controlled by a workstation PC (Intel Core i7-5930K CPU at 3.50 GHz, 32 GB RAM) running a custom magnetic control program written in C++. The Fourier transform-based reconstruction and the variance calculation is implemented on a GPU using compute unified device architecture (CUDA) for parallel computations. Under the current configurations of the system, the tracking algorithm can process images at 40 Hz (each step in Section III respectively takes 7.0 ms, 16.0 ms, and 1.3 ms on average). To provide a buffer, the image acquisition and control loop is limited to 20 Hz in the demonstrations.

B. System Calibration

The accuracy of the tracking algorithm is tested using a motorized stage (resolution of 1 nm) controlling the 3D position of the calibration probe. The same NdFeB cylindrical magnet used for the control experiments is attached to a 22 μm diameter tungsten wire. First, the axial position estimation is investigated. The calibration probe is moved in the axial direction in steps of 200 μm within the 10 mm propagation range in air. Fig. 6 (a, top) shows the relation between the actual and focused depth, which is obtained from the tracking algorithm. The slope of this line is the effective refractive index of the medium. Using least squares, the refractive index of air is measured to be 1.006 and the standard deviation of the residuals is 62.47 μm [in Fig. 6 (a, top)]. The same procedure is performed to experimentally determine the refractive index of the silicone oil and to calibrate the system. The calibration probe is moved at intervals of 200 μm within the 5 mm propagation range in the silicone oil. We observe the refractive index of silicone oil as 1.633 and the expected axial tracking accuracy in silicone oil as 61.93 μm (in Fig. 6 (b, top)).

Second, the accuracy of the 3D position estimate is investigated by moving the probe in 3D (in Fig. 6 (a, b, bottom)). The reference trajectory is three 4 mm squares at a depth of -2, 0, and 2 mm. Using least squares [34], the optimal rotation and translation is found to eliminate the effect of misalignment between the camera and the stage. The standard deviations of residuals are 0.018 mm, 0.062 mm, and 0.014 mm in air, and 0.023 mm, 0.169 mm, and 0.014 mm in silicone oil, for x-, y-, and z-axes, respectively. As expected from (6), the in-plane estimation shows smaller tracking errors than in the depth direction.

The calibration is investigated by moving the probe along a cubic trajectory, which is discretized in 500 μm steps (in Fig. 6(c)). Along the x- and z-axes, the standard deviations of the tracking error are 0.017 mm and 0.015 mm, which are approximately three camera pixels. Along the y-axis, we observe a tracking error of 0.189 mm, which is comparable to the axial resolution of the system calculated as 0.181 mm within the workspace using (6).
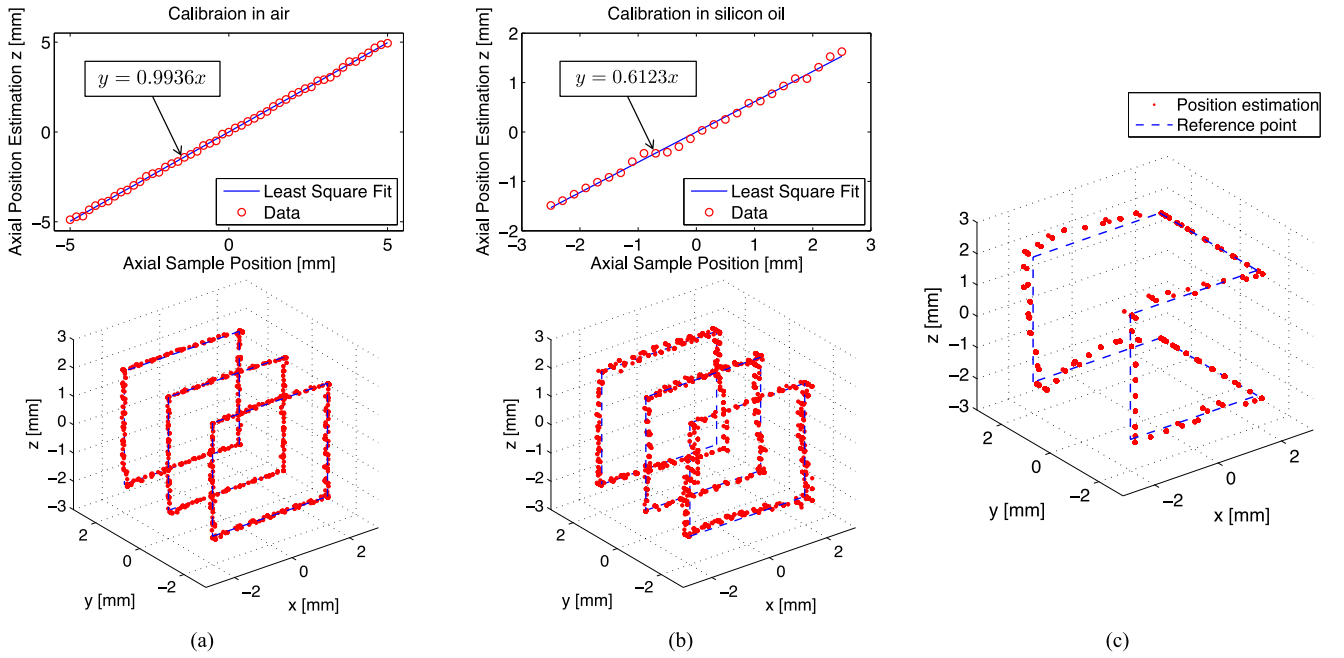
Fig. 6. Accuracy of the proposed tracking algorithm is tested with a motorized stage controlling the 3D position of the NdFeB cylinder magnet with a diameter of 500 μm and a height of 500 μm. (a, b) (top) Axial position estimation is determined in air and silicone oil. The refractive indices of air and silicone oil are estimated as 1.006 and 1.633. (bottom) 3D position estimation is determined using a reference trajectory with 4 mm squares in $y = (-2, 0, 2)$ mm. The standard deviations of residuals are 0.018 mm, 0.062 mm, and 0.014 mm in air, and 0.023 mm, 0.169 mm, and 0.014 mm in silicone oil, along the x-, y-, and z-axes. (c) The calibration probe is moved along a 4 mm cube trajectory as in control experiments with 500 μm of a step size. The standard deviations of the tracking error are 0.017 mm, 0.189 mm, and 0.015 mm for x-, y-, and z-axes.
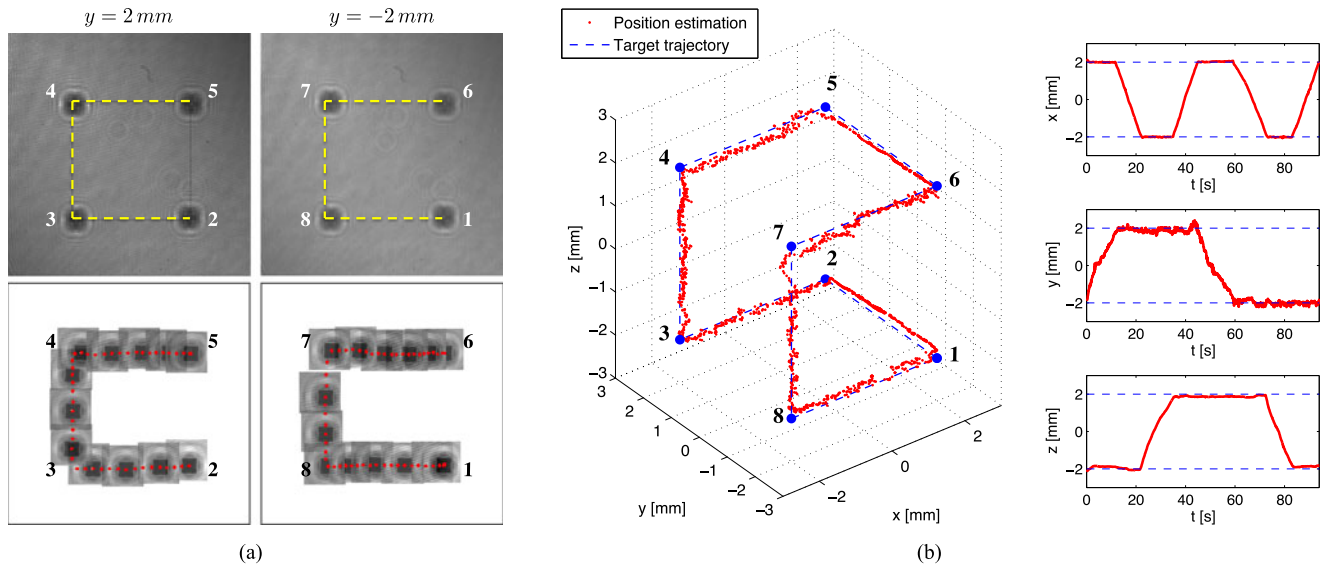

Fig. 7. Demonstration of 3D closed-loop position control using holographic tracking. The target trajectory is a 4 mm cube at the center of the workspace following the vertices from 1 to 8. A PD controller is used to minimize the position error between the estimation and the target point, which is 0.3 mm ahead of the projection in the target trajectory. (a) Composite images of the captured hologram h_0 show the microrobot at the trajectory vertices in $y = 2$ mm and $y = -2$ mm. The yellow line shows the target trajectory. The time-lapse images at the bottom show the focused image $|h_2|$ located at the position estimation for every 80 frames. The position estimation is indicated with a red dot in every 20 frames. (b) The 3D trajectory and tracking positions used for the controller are presented for one-cycle of trajectory. The mean tracking errors are -0.004 mm, 0.088 mm, and 0.060 mm, and the standard deviations are 0.022 mm, 0.125 mm, and 0.101 mm in x-, y-, and z-axes for five cycles of trajectory. The trajectory completion time is 89 s on average.

C. 3D Closed-Loop Position Control

The estimated 3D position is used as a measurement input for a closed-loop feedback-linearizing controller that calculates the magnetic fields necessary to move the NdFeB magnet along a desired trajectory [5]. The target trajectory is a 4 mm cube centered in the workspace (in Fig. 7(b)). At a given step, the desired target position is defined to be 0.3 mm ahead of the projection of the current position of the microrobot on the target trajectory. The position estimate is filtered using a discrete forth-order low-pass butterworth filter with a 0.33 π rad/sample cutoff

frequency. In the experiment, the microrobot is aligned with the z-axis.

The tracking position estimates used for the controller are reported in 3D for a single trajectory (in Fig. 7(b)). The tracking error of 0.022 mm along x is approximately four camera pixels, agreeing with the calibration result. The tracking error of 0.101 mm along z is four times larger than that in calibration which we attribute to errors in the gravity compensation of the microrobot. As expected, the tracking is less precise in the depth direction y with an error of 0.125 mm.

V. CONCLUSION AND DISCUSSION

This paper demonstrates real-time 3D position tracking of microrobots using digital holography in a microrobot control application. The advantages of holography over conventional optical microscopy for real-time tracking include the compactness of the imaging system, the ability to image the scene without requiring manual or automated mechanical focusing, and the ability to estimate an objects's out-of-plane position along with its in-plane position from a single image. An additional advantage of holography for imaging microscale systems comes from object segmentation. Traditionally, small objects are difficult to segment from large backgrounds because they are difficult to distinguish from noise. However, in a holographic image, small objects affect a much larger region of the image than their physical extent because the technique considers diffraction patterns rather than reflections or shadows. For example, Fig. 4 shows that even very small objects can be clearly identified in raw holography images. This allows for smaller devices in larger workspaces without significant losses of resolution.

Although the cylindrical magnet is presented as a microdevice in this paper, the proposed tracking method can be extended to other shapes of microdevices, such as artificial bacterial flagella [2], or be used with nonmagnetic control systems. The method could also be adapted to track 3D position as well as 3D orientation of a single or multiple agents albeit at an increased computational cost.

REFERENCES

[1] B. J. Nelson, I. K. Kaliakatsos, and J. J. Abbott, "Microrobots for minimally invasive medicine," *Annu. Rev. Biomed. Eng.*, vol. 12, pp. 55–85, 2010.

[2] L. Zhang, K. E. Peyer, and B. J. Nelson, "Artificial bacterial flagella for micromanipulation," *Lab Chip*, vol. 10, no. 17, pp. 2203–2215, 2010.

[3] E. Diller and M. Sitti, "Three-dimensional programmable assembly by untethered magnetic robotic micro-grippers," *Adv. Function Mater.*, vol. 24, no. 28, pp. 4397–4404, 2014.

[4] D. Ahmed *et al.*, "Rotational manipulation of single cells and organisms using acoustic waves," *Nature Commun.*, vol. 7, 2016, Art. no. 11085.

[5] M. P. Kummer, J. J. Abbott, B. E. Kratochvil, R. Borer, A. Sengul, and B. J. Nelson, "OctoMag: An electromagnetic system for 5-dof wireless micromanipulation," *IEEE Trans. Robot.*, vol. 26, no. 6, pp. 1006–1017, Dec. 2010.

[6] S. Schürle, S. Erni, M. Flink, B. E. Kratochvil, and B. J. Nelson, "Three-dimensional magnetic manipulation of micro-and nanostructures for applications in life sciences," *IEEE Trans. Magn.*, vol. 49, no. 1, pp. 321–330, Jan. 2013.

[7] E. Diller, J. Giltinan, and M. Sitti, "Independent control of multiple magnetic microrobots in three dimensions," *Int. J. Robot. Res.*, vol. 32, no. 5, pp. 614–631, 2013.

[8] I. S. Khalil, V. Magdanz, S. Sanchez, O. G. Schmidt, and S. Misra, "Three-dimensional closed-loop control of self-propelled microjets," *Appl. Phys. Lett.*, vol. 103, no. 17, 2013, Art. no. 172404.

[9] P. J. Rodrigo, V. R. Daria, and J. Glückstad, "Four-dimensional optical manipulation of colloidal particles," *Appl. Phys. Lett.*, vol. 86, no. 7, 2005, Art. no. 074103.

[10] H. Marino, C. Bergeles, and B. J. Nelson, "Robust electromagnetic control of microrobots under force and localization uncertainties," *IEEE Trans. Autom. Sci. Eng.*, vol. 11, no. 1, pp. 310–316, Jan. 2014.

[11] P. Ferraro *et al.*, "Extended focused image in microscopy by digital holography," *Opt. Express*, vol. 13, no. 18, pp. 6738–6749, 2005.

[12] P. Grossmann, "Depth from focus," *Pattern Recog. Lett.*, vol. 5, no. 1, pp. 63–69, 1987.

[13] Z. Zhang and C.-H. Menq, "Three-dimensional particle tracking with subnanometer resolution using off-focus images," *Appl. Opt.*, vol. 47, no. 13, pp. 2361–2370, 2008.

[14] J. Garcia-Sucerquia, W. Xu, S. K. Jericho, P. Klages, M. H. Jericho, and H. J. Kreuzer, "Digital in-line holographic microscopy," *Appl. Opt.*, vol. 45, no. 5, 2006, Art. no. 836.

[15] T. Latychevskaia and H.-W. Fink, "Practical algorithms for simulation and reconstruction of digital in-line holograms," *Appl. Opt.*, vol. 54, no. 9, pp. 2424–2434, Mar. 2015.

[16] D. Gabor, "A new microscopic principle," *Nature*, vol. 161, no. 4098, pp. 777–778, 1948.

[17] W. S. Haddad *et al.*, "Fourier-transform holographic microscope," *Appl. Opt.*, vol. 31, no. 24, pp. 4973–4978, 1992.

[18] M. F. Toy, S. Richard, J. Kühn, A. Franco-Obregón, M. Egli, and C. Depeursinge, "Enhanced robustness digital holographic microscopy for demanding environment of space biology," *Biomed. Opt. Express*, vol. 3, no. 2, pp. 313–326, Feb. 2012.

[19] F. Merola *et al.*, "Digital holography as a method for 3D imaging and estimating the biovolume of motile cells," *Lab. Chip*, vol. 13, no. 23, pp. 4512–4516, 2013.

[20] P. Memmolo, A. Finizio, M. Paturzo, L. Miccio, and P. Ferraro, "Twin-beams digital holography for 3d tracking and quantitative phase-contrast microscopy in microfluidics," *Opt. Express*, vol. 19, no. 25, pp. 25 833–25 842, 2011.

[21] I. Pushkarsky *et al.*, "Automated single-cell motility analysis on a chip using lensfree microscopy," *Sci. Rep.*, vol. 4, 2014, Art. no. 4717.

[22] M. Heydt, A. Rosenhahn, M. Grunze, M. Pettitt, M. Callow, and J. Callow, "Digital in-line holography as a three-dimensional tool to study motile marine organisms during their exploration of surfaces," *J. Adhesion*, vol. 83, no. 5, pp. 417–430, 2007.

[23] L. Tian, N. Loomis, J. A. Domínguez-Caballero, and G. Barbastathis, "Quantitative measurement of size and three-dimensional position of fast-moving bubbles in air-water mixture flows using digital holography," *Appl. Opt.*, vol. 49, no. 9, pp. 1549–1554, Mar. 2010.

[24] J. Fung, K. E. Martin, R. W. Perry, D. M. Kaz, R. McGorty, and V. N. Manoharan, "Measuring translational, rotational, and vibrational dynamics in colloids with digital holographic microscopy," *Opt. Express*, vol. 19, no. 9, pp. 8051–8065, Apr. 2011.

[25] M. F. Toy, J. Kühn, S. Richard, and J. Parent, "Accelerated autofocusing of off-axis holograms using critical sampling," *Opt. Lett.*, vol. 37, no. 24, pp. 5094–5096, 2012.

[26] H. A. İlhan, M. Doğar, and M. Özcan, "Fast autofocusing in digital holography using scaled holograms," *Opt. Commun.*, vol. 287, pp. 81–84, 2013.

[27] T. Shimobaba, Y. Sato, J. Miura, M. Takenouchi, and T. Ito, "Real-time digital holographic microscopy using the graphic processing unit," *Opt. Express*, vol. 16, no. 16, pp. 11 776–11 781, Aug. 2008.

[28] M. Doğar, H. A. İlhan, and M. Özcan, "Real-time, auto-focusing digital holographic microscope using graphics processors," *Rev. Sci. Instrum.*, vol. 84, no. 8, 2013, Art. no. 083704.

[29] U. Schnars and W. P. O. Jüptner, "Digital recording and numerical reconstruction of holograms," *Meas. Sci. Technol.*, vol. 13, no. 9, 2002, Art. no. R85.

[30] T. M. Kreis, M. Adams, and W. P. Jueptner, "Digital in-line holography in particle measurement," in *Proc. Int. Conf. Opt. Metrology*, 1999, pp. 54–64.

[31] N. Demoli, J. Meštrović, and I. Sović, "Subtraction digital holography," *Appl. Opt.*, vol. 42, no. 5, pp. 798–804, 2003.

[32] G. Pan and H. Meng, "Digital holography of particle fields: Reconstruction by use of complex amplitude," *Appl. Opt.*, vol. 42, no. 5, pp. 827–833, 2003.

[33] R. P. Brent, *Algorithms for Minimization Without Derivatives*. North Chelmsford, MA, USA: Courier Corporation, 2013.

[34] B. Zitova and J. Flusser, "Image registration methods: A survey," *Image Vis. Comput.*, vol. 21, no. 11, pp. 977–1000, 2003.